Chinese Chemical Letters 37 (2026) 111412

Contents lists available at ScienceDirect

Chinese Chemical Letters

journal homepage: www.elsevier.com/locate/cclet

Giant 28-nuclear water cluster-intercalated polyoxometalate-based photocatalyst with bandgap modulation for efficient CO_2 photoconversion

Yin-Hua Zhu, Yong-Qi Ji, Jian-Bo Yang, Xin-Ying Xiang, Hua Mei*, Yan Xu*

College of Chemical Engineering, State Key Laboratory of Materials-Oriented Chemical Engineering, Nanjing Tech University, Nanjing 211816, China

ARTICLE INFO

Article history:
Received 29 March 2025
Revised 26 May 2025
Accepted 6 June 2025
Available online 6 June 2025

Keywords:
Reduced polyoxometalate-based catalyst
Photocatalytic CO_2 reduction
Water intercalation
Band gap regulation
Heterogeneous catalyst

ABSTRACT

Guest molecule intercalation is an effective strategy for engineering electron structures and enhancing photocatalytic CO_2 reduction. Our designed charge-transfer system incorporates 28 nuclear H_2O molecules as electron mediators within the POM-based photocatalyst, enabling efficient electron transport pathways. Comparative analysis of synthesized isostructural catalysts shows water-intercalated $Na_7[Co_2(H_2O)_8(H_{11}CoP_8Mo_{12}O_{62})]\cdot 44H_2O$ (abbr. compound **1**) achieves exceptional CO_2 reduction activity ($21{,}347.4\ \mu mol\ g^{-1}\ h^{-1}$), outperforming anhydrous $(C_4H_{14}N_2)_4[Co_2(H_{10}CoP_8Mo_{12}O_{62})]\cdot 4H_2O$ (abbr. compound **2**) by 68 %. This work demonstrates that water intercalation simultaneously optimizes band structure and improves material stability, providing a novel paradigm for advanced photocatalytic system design.

© 2026 Published by Elsevier B.V. on behalf of Chinese Chemical Society and Institute of Materia Medica, Chinese Academy of Medical Sciences.

The relentless combustion of fossil fuels has precipitated a substantial surge in carbon dioxide (CO_2) emissions, resulting in both environmental degradation and energy scarcity on a global scale [1–4]. A promising solution to this critical challenge lies in the photocatalytic reduction of CO_2 (PCO_2RR) into value-added chemicals, mimicking the efficiency of natural photosynthesis [5–8]. However, the chemical inertness of CO_2 limits the activity and selectivity of photocatalysts, posing a major obstacle to improving the efficiency of photocatalysis. To overcome these obstacles, developing advanced photocatalysts is essential [9–11].

Polyoxometalates (POMs) have become staples in various applications ranging from catalysis to energy storage and conversion [12–14]. Their widespread adoption is attributed to their exceptional performance from their well-defined and customizable structures. In particular, they are used as excellent solid conductors due to their abundant electron redox capacity, high lattice oxygen activity, and strong proton acidity. Among POMs, the hourglass polyanion $\{M[P_4Mo_6{}^{V}O_{31}]_2\}^{n-}$ (abbreviated $\{M[P_4Mo_6]_2\}$) is particularly noteworthy; it is formed by a central metal (M^{n+}) connecting two $[P_4Mo_6{}^{V}O_{31}]^{12-}$ units (abbreviated $\{P_4Mo_6\}$) [15–17]. These $\{P_4Mo_6\}$ clusters exhibit unique redox properties, with all Mo centers at +5 oxidation state, indicating that this natural hetero-poly blue possesses stronger photon absorption and redox capacity than classical Keggin- and Dawson-type clusters [18,19]. However, the solubility of monomer POM clusters has been a significant limiting factor for catalytic durability. Therefore, a stable structure is a prerequisite for applying POM chemistry in heterogeneous catalysis [20–23].

Density functional theory (DFT) studies have reported that the embedding of guest molecules (N_2, Xe, CO, H_2O) into structures can lead to a narrow band gap, however, not enough attention has been paid to the structural changes that occur when water is embedded into POM-based hybrid materials and their effects on photocatalytic performance [24–27]. This arrangement not only improves charge transfer efficiency but also reduces the electronic bandgap of the catalyst, leading to increased conductivity and enhanced charge separation, which are essential for effective photocatalysis [28–34]. The effects of intercalated water molecules provide an effective strategy for enhancing both the efficiency and stability of photocatalysts, making significant strides in CO_2 reduction and energy conversion applications.

Using a comprehensive suite of characterization techniques, including single-crystal X-ray diffraction (SCXRD), powder X-ray diffraction (PXRD), and Fourier-transform infrared spectroscopy (FT-IR). We proved that the giant 28-nuclear water cluster-intercalated compound $Na_6(H_3O)_6[Co(H_2O)_4]_2\{Co[Mo_6O_{12}(OH)_3(PO_4)_4]_2\}\cdot 40H_2O$ (**1**) the success of the preparation. For comparative analyses, we also prepared a similar anhydrous intercalated catalyst **2**,

* Corresponding authors.
E-mail addresses: meihua@njtech.edu.cn (H. Mei), yanxu@njtech.edu.cn (Y. Xu).

https://doi.org/10.1016/j.cclet.2025.111412
1001-8417/© 2026 Published by Elsevier B.V. on behalf of Chinese Chemical Society and Institute of Materia Medica, Chinese Academy of Medical Sciences.

$[H_3N(CH_2)_4NH_3]_4(CoH_2O)_2\{Co[Mo_6O_{12}(OH)_3(HPO_4)_2(PO_4)_2]_2\}\cdot 2H_2O$ (**2**). Significantly, under visible light irradiation, catalyst **1** demonstrated exceptional photocatalytic activity, with a CO_2 generation rate of 21,347.4 μmol g^{-1} h^{-1}, approximately 1.68 times that of catalyst **2**, highlighting its potential in developing efficient photocatalysts. We further examined the intricate relationships between structural characteristics and key properties, including DFT calculation, optical band gaps, charge separation efficiency, and chemical stability. The data obtained from ultraviolet-visible (UV–vis) spectroscopy, electrochemical impedance spectroscopy (EIS), photocurrent response (*I-t*), and steady-state photoluminescence (PL) spectra support our hypotheses.

SCXRD demonstrates that compound **1** adopts a monoclinic crystal structure, belonging to the *C*2/*m* space group. The basic unit consists of two $\{P_4Mo_6\}$ POM anion clusters, three Co^{2+} cations, seven Na^+ cations, and several coordinated H_2O, free H_2O molecules. The Mo–O bond lengths range from 1.685(4) Å to 2.285(4) Å, and the O–Mo–O bond Angle ranges from 73.03(14)° to 170.46(17)° with an average bond angle of about 107.2°. The lengths of the P–O bonds vary between 1.508(5) Å and 1.572(5) Å, while the O–P–O bond angles vary from 105.9(2)° to 113.2(4)°.

In compound **1**, Co^{2+} adopts two crystallographically independent Co. In the first mode, Co1 is six-coordinated, forming bonds with six μ_3-oxygen atoms (O2, O4) from two $\{P_4Mo_6\}$ POM clusters, resulting in the formation of a classical "sandwich" structure (Fig. 1a). The Co1–O bond lengths range from 2.135(4) Å to 2.166(5) Å. In the second mode, Co2 is also six-coordinated, with two O atoms derived from distinct $\{P_4Mo_6\}$ POM anion clusters (O18), while the remaining four oxygens are supplied by coordinated water molecules (O1w, O3w). The Co2–O bond lengths range from 2.077(4) Å to 2.146(4) Å. The adjacent $\{Co[Mo_6O_{12}(OH)_3(PO_4)_4]_2\}^{16-}$ POM anion clusters are interconnected *via* four $\{CoO_6\}$ octahedra, forming a 22-membered ring structure (Fig. 1b). These 22-membered rings are further interconnected, resulting in the formation of an inorganic POM framework. In between the POM layers, a lot of water molecules remain free.

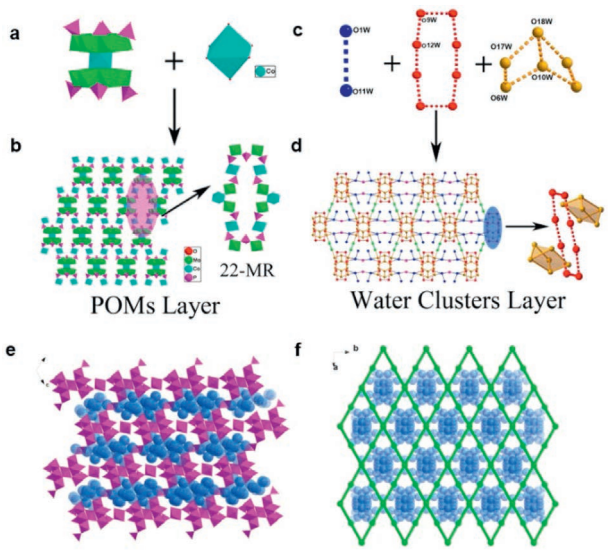


Fig. 1. (a, b) The POM layer is composed of $\{P_4Mo_6\}$ unit and cobalt ions. (c, d) A water layer consisting of twenty-eight nucleated H_2O clusters and free H_2O in **1**. (e) The way water and POM layers are stacked along the *b* axis of **1** (the blue ball represents the water layer and the purple polyhedron represents the POM layer). (f) The way water and POM layers are stacked along the *c*-axis in compound **1** (the green ball-stick diagram represents the POM layer and the blue ball represents the water layer).

There are three different configurations of water clusters by analyzing the distance and angle between water molecules (Fig. 1c). The dimeric water cluster, formed by O1w and O11w through hydrogen bonding, exhibits an O···O distance of 2.788 Å, in agreement with previously reported compounds. The hexanuclear water cluster displays a typical "book" configuration, with an average O···O distance of 2.75 Å. The eight-core water in compound **1** deviates from the classical structure, adopting a rectangular arrangement where two O9w atoms form the shorter sides, and the longer side consists of a linear chain of O9w···O12w···O12w···O9w. The average O···O distance within the eight-core water is 2.94 Å. As depicted in Fig. 1d, two "book"-type hexanuclear water clusters are situated on either side of the eight-core water and are linked by hydrogen bonds to four dimeric water clusters, forming a giant $(H_2O)_{28}$ water cluster. This $(H_2O)_{28}$ water cluster is further connected *via* free water molecules (O3w, O20w), giving rise to a unique water layer (Fig. 1e). Adjacent water layers interact through hydrogen bonds to form a 3D supramolecular structure (Fig. 1f). Although many hydrous cluster compounds have been reported, most of these clusters remain isolated, and only a few exhibit interactions between clusters to form infinite networks.

According to SCXRD studies, compound **2** has an analogous molecular structure resembling compound **1** and crystallizes in the triclinic system, P$\bar{1}$ space group. The basic unit of compound **2** was composed of two $\{P_4Mo_6\}$ anion clusters, three Co^{2+} ions, four protonated 1,4-butane-diamine (BDA) molecules, and several coordinated free water molecules (Fig. S5 in Supporting information). The Mo–O bond lengths vary between 1.675(5) Å to 2.296(5) Å, and the O–Mo–O bond Angle ranges from 72.58(17)° to 169.8(2)° with an average bond angle of about 97.4°. Similarly, in compound **2**, the Co^{2+} ion exhibits two different coordination patterns (Fig. S4 in Supporting information). The first is represented as Co1, which is hexagonal and joined with six μ_3-O atoms (O1, O2, O6) in two $\{P_4Mo_6\}$ anion clusters, thus forming a classic "sandwich" structure. The bond length of Co1–O ranges from 2.050(3) Å to 2.205(3) Å. The second type of Co2 is pentacoordination, which is attached to five oxygen atoms. Four oxygen atoms came from three adjacent $\{P_4Mo_6\}$ anion clusters (O19, O12, O26, O10), while the fifth O atom was supplied by the coordinated water molecule (O32). The bond length of Co2–O is also between 2.050(3) Å and 2.205(3) Å. The two adjacent $\{Co(P_4Mo_6O_3)\}$ units are connected by two $\{CoO_5\}$ tetrahedra, forming a twelvefold ring. The $\{Co_2P_2\}$ four-membered rings further connect these twelve rings, creating an interesting layered architecture. Two neighboring inorganic layers are separated by protonated 1,4-butane diamine molecules, joined to the inorganic layer *via* hydrogen bonds. "Layer A-Layer B" is the arrangement of two neighboring inorganic layers that are not entirely congruent but alternate and staggered.

The PXRD pattern for compound **1** closely aligns with the theoretical values derived from SCXRD, thereby attesting to the sample's high purity. The FT-IR spectra of compounds **1** and **2** within the 4000–400 cm^{-1} range are depicted in Figs. S6 and S7 (Supoprting information). Because of the structural water in compound **1**, the O–H stretching vibration band for compound **1**, located at 3423 cm^{-1}, looks wider than that of compound **2**, located at 3447 cm^{-1}. Within compound **1**, the peak at 1633 cm^{-1} signifies the in-plane bending vibration of the O–H group, whereas the peak at 950 cm^{-1} corresponds to the stretching vibration of the Mo=O bond. The Mo–O–Mo linkage's vibrations are responsible for the band at 730 cm^{-1}, whereas the peak indicates the P–O bond's stretching vibration at 1043 cm^{-1}. Concerning compound **2**, the distinctive peaks located at 1609 and 961 cm^{-1} signify the stretching vibration of Mo=O and the in-plane bending vibration of O–H, respectively. Vibrations associated with the Mo–O–Mo bond are ascribed to the band at 738 cm^{-1}, whereas the peak indicates the vibrations caused by stretching of the P–O bond at 1057 cm^{-1}.

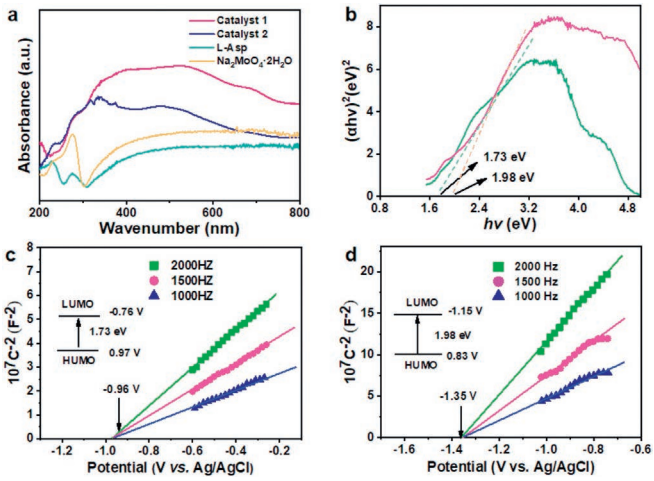


Fig. 2. (a) Solid UV–vis spectra of compounds **1** and **2** and part of the reaction feedstock. (b) Tauc plots of compounds **1** and **2**. (c, d) Mott-Schottky plots for **1** and **2**.

A thorough investigation of their UV–vis spectra was conducted to assess the visible light absorption capabilities and electronic band structure of compounds **1** and **2**. The absorption spectra within the 200–800 nm range were captured and are depicted in Fig. 2a. Reaction materials $Na_2MoO_4{\cdot}2H_2O$ and L-aspartic acid (L-Asp) have poor absorption in the visible region. It is observed that compound **1** exhibits a broader absorption intensity in the visible light region compared to compound **2**, which may be attributed to the incorporation of water clusters that enhance the compound's capacity to absorb a greater fraction of the solar spectrum. Utilizing the Kubelka-Munk equation ($\alpha h\nu = C(h\nu - E_g)^{1/2}$), the band gap ($E_g$) of compound **1** was determined to be 1.73 eV, while that of compound **2** is 1.98 eV in Fig. 2b. Mott-Schottky (MS) test at 1000, 1500, and 2000 Hz was performed, with the positive slope of the resulting curves further confirming the N-type semiconductor characteristics (Figs. 2c and d). Given that the conduction band of an N-type semiconductor is near its flat band potential, the LUMO potentials of compounds **1** and **2** relative to the Ag/AgCl electrode were determined to be −0.96 and −1.35 eV, respectively.

Upon conversion to the standard hydrogen electrode (NHE) reference, the LUMO positions for compounds **1** and **2** are adjusted to −0.76 and −1.15 eV, respectively. Correspondingly, the HOMO positions for these compounds are calculated to be 0.97 and 0.83 eV, respectively. The reduction potential for CO_2 photoreduction for each product falls between the HOMO and LUMO bands of compounds **1–2**, suggesting that high-energy electrons injected onto the surface of compounds **1** and **2** are poised to reduce CO_2. Structurally, the inclination angle of O–Mo–O in compound **1** is significantly larger than in compound **2**, indicating a substantial correlation between the inclination angle and the band gap. This correlation may arise from the increased overlap between the Mo 4d and O 2p orbitals due to the increased tilt angle, leading to enhanced conduction band dispersion and a consequent positive shift [35].

The photocatalytic CO_2 reduction experiment was conducted in a CO_2-saturated mixed solution (MeCN:TEOA = 4:1, v/v) using $[Ru(bpy)_3]Cl_2{\cdot}6H_2O$ as the photosensitizer (PS). A mixture of gaseous CO and H_2 was detected by gas chromatography. No liquid by-product was produced during the entire reaction. The photocatalytic system, employing 10 mg of compounds **1** and **2** as heterogeneous catalysts **1** and **2**, exhibited notable CO_2 conversion efficiency, producing 277.8 μmol of CO for catalyst **1** and 104.8 μmol for **2** within 8 h (Fig. 3a). Catalyst **1** exhibits superior catalytic activity compared to **2**, hence, further detailed investigation of the photocatalytic performance of catalyst **1** is warranted.

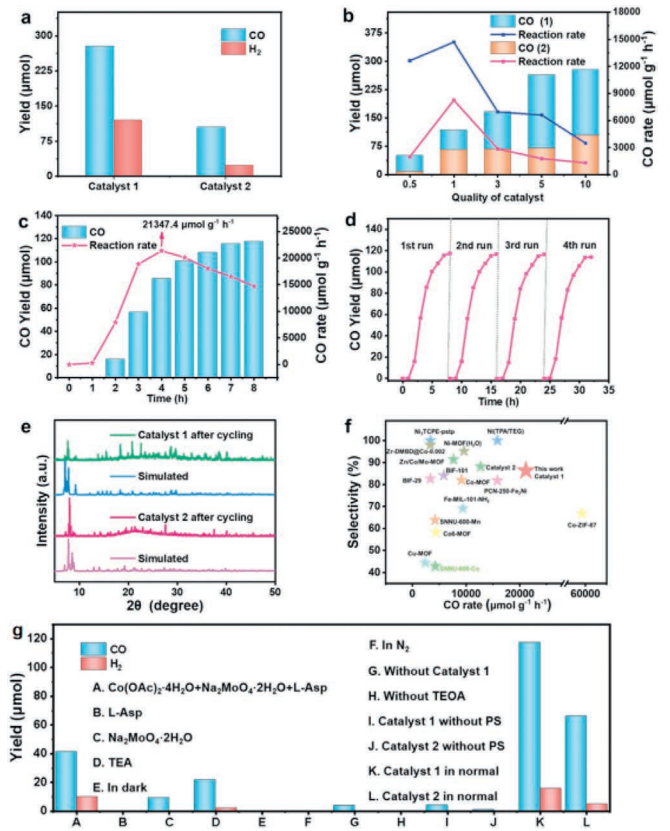


Fig. 3. (a) Comparison of the performance of catalyst **1** and **2**. (b) Dose effect on catalyst **1** and **2**. (c) The change of the performance of catalyst **1** with reaction time. (d) The performance of catalyst **1** after four recoveries and dispersions. (e) PXRD patterns of compounds **1** and **2** after cyclic experiments. (f) Comparison of the performance of catalysts **1** and **2** with some advanced photocatalysts. (g) The role of different components in the photocatalytic system.

To achieve greater economic benefits, the impact of the optimal amount of catalyst **1** on photocatalysis was further studied (Fig. 3b). The trend curve for the target product CO of **1** exhibits a "volcano-like" pattern. When the mass of catalyst **1** was reduced to 0.5 mg, the total CO yield significantly dropped to 50.5 μmol, with a productivity rate of 12,632.0 μmol g^{-1} h^{-1}. Further increasing the catalyst **1** to 1 mg, the CO yield reached 117.5 μmol, with a productivity rate of 14,689.9 μmol g^{-1} h^{-1}. Significantly, catalyst **1** outperforms some of the most advanced catalysts, including Ni(TPA/TEG), Ni-MOF, and Zn/Co/Mo-MOF in the CO_2RR process (Fig. 3f). This outcome is better than the majority of reported photocatalysts. Table S3 (Supporting information) presents the findings. This remarkable performance underscores the exceptional catalytic efficiency of catalyst **1**. Specifically, Fig. 3c displays the time curve of CO evolution and rate when using 1 mg of catalyst **1** as a photocatalyst. It is important to observe that the CO production rate peaked at 21,347.4 μmol g^{-1} h^{-1} within 4 h. However, as the irradiation period extended, the rate of CO generation experienced a linear decline, attributed to the inadequate transfer of photoelectrons from the photosensitizer to catalyst **1**. Further increasing the catalyst amount to 3 or 5 mg, the CO yield increased to 167.0 μmol and 264.2 μmol, respectively. Still, the corresponding formation rates sharply decreased to only 6959.0 and 6605.3 μmol g^{-1} h^{-1}. This may be limited by the electron transfer kinetics, resulting in the excess catalyst not functioning effectively.

The reusability and stability of the catalyst are also important indices for evaluating the catalytic performance. Remarkably, even

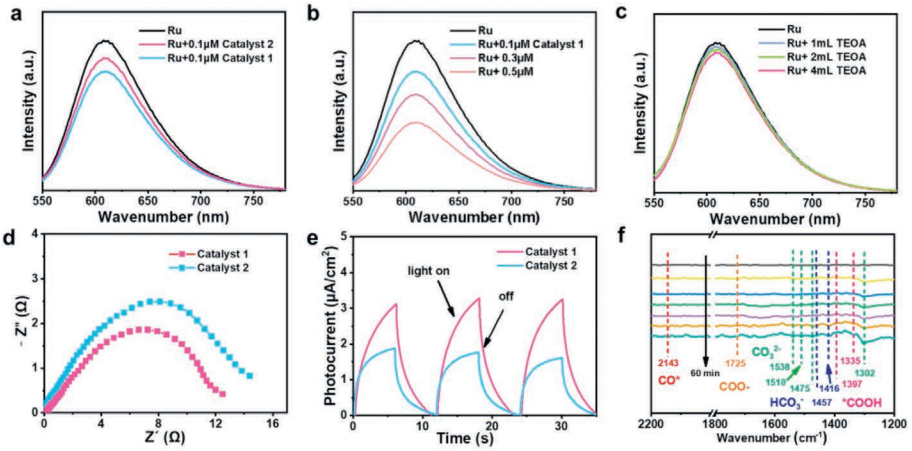


Fig. 4. PL spectra of PS in MeCN solution with (a) different catalyst, (b) different catalyst **1** dosage, and (c) different TEOA dosage. (d) Electrochemical impedance spectra and (e) photocurrent responses under UV–vis illumination of **1** and **2**. (f) *In-situ* FT-IR spectra for the adsorption and photocatalytic activation of CO_2 on **1**.

after four cycles of use, catalyst **1** shows no significant loss in its ability to produce CO, which indicates that its original activity is well preserved (Fig. 3d). Furthermore, any slight decrease in CO yield observed could be due to minor sample mass loss, a common occurrence in such processes.

Moreover, the PXRD patterns of catalyst **1** post-photocatalytic reactions agree with those of the fresh catalyst (Fig. 3e). This consistency validates the catalyst's structural stability throughout the photocatalytic process, ensuring its reliability and longevity in practical applications.

We conducted comparative experiments to explore how reaction conditions affect photocatalytic performance, with key findings in Fig. 3g. Results show that light, photosensitizer PS, and TEOA are crucial for CO_2 reduction, with TEOA enhancing conversion by providing electrons and stabilizing/activating CO_2. The catalyst **1**′s ordered framework, uniform exposure of active units, and cobalt's synergistic effect significantly boost photocatalytic CO_2 reduction efficiency.

To decipher the mechanism of photoexcited charge transfer, we conducted PL quenching experiments in an acetonitrile solution enriched with PS (Figs. 4a–c). It is worth noting that the quenching effect of catalyst **1** is more obvious than that of catalyst **2**, and the quenching effect is more obvious with the increase of catalyst dosage. Moreover, the quenching effect of TEOA on the PS was markedly less than that induced by the catalyst. Collectively, these observations imply that the fluorescence quenching is linked to the superior efficiency of PS in facilitating charge transfer at the catalyst surface. Furthermore, in the transient photocurrent response curve (*I-t*), catalyst **1** exhibits sharp and sensitive photocurrent spikes, indicating its better ability to separate photogenerated electron-hole pairs (Fig. 4e). This enhanced response suggests more efficient charge transfer to the catalyst surface for photocatalytic reactions. The smaller semicircular radius of the Nyquist diagram indicates that the charge transfer impedance of the sample is reduced, reflecting the faster photogenerated charge transfer by water intercalation engineering (Fig. 4d).

To evaluate the specific process of catalyst **1** as a photocatalyst in the PCO_2RR, *in situ* FT-IR was employed under a CO_2 atmosphere (Fig. 4f). After 60 min of light irradiation, the spectrum exhibited distinct characteristic peaks. Peaks located at 1416 and 1457 cm^{-1} were identified as belonging to the bicarbonate (HCO_3^-) group, while the absorption peak at 1725 cm^{-1} is attributed to the carbonate (COO^-) species. Peaks at 1475 and 1510 cm^{-1} were confirmed as corresponding to the carbonate (CO_3^{2-}) group, and the absorption peak at 1725 cm^{-1} is also attributed to the carbonate (COO^-) species. Notably, the peaks around 1397 and 1335 cm^{-1} are

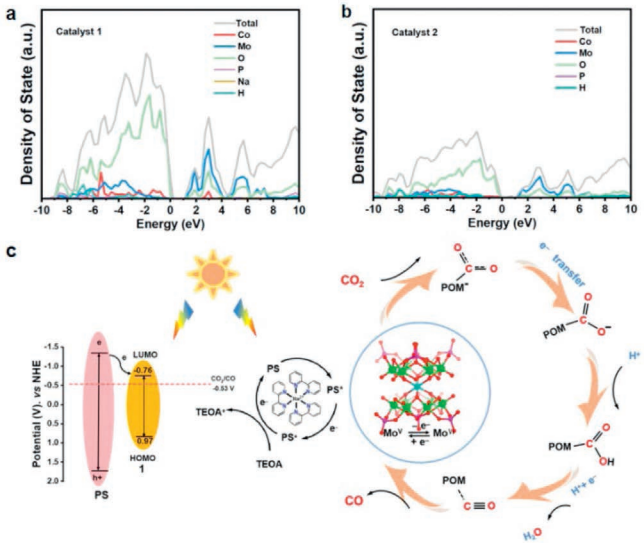


Fig. 5. (a) DFT-computed DOS of catalyst **1**. (b) DFT-computed DOS of catalyst **2**. (c) The proposed reaction mechanism for converting CO_2 to CO *via* photocatalysis.

associated with the carboxylic acid (COOH) group, which is considered an intermediate in the reduction of CO_2 to CO. The peak of the CO* species at 2143 cm^{-1} supports the formation of CO during the photocatalytic reduction of CO_2.

DFT calculations reveal the band structures of water-intercalated catalyst **1** and anhydrous catalyst **2** (Figs. 5a and b). Catalyst **1** shows a narrowed theoretical bandgap (0.87 eV *vs.* experimental 1.73 eV) with VBM and CBM positive shifts. In comparison, catalyst **2** exhibits a 1.09 eV computed bandgap (experimental 1.98 eV), consistent with DFT's inherent bandgap underestimation [36,37]. PDOS analysis demonstrates that catalyst **1**′s CBM comprises O 2p and Mo 4d orbitals, *versus* VBM dominated by O 2p orbitals. This configuration enables photogenerated electron transfer from the water intercalation layer's O 2p to Mo 4d orbitals. Notably, water intercalation enhances O 2p orbital contribution by 38 % in the valence band compared to catalyst **2**, confirming its pivotal role in electronic structure modulation.

Based on the above experiments and literature, a reasonable reaction mechanism was deduced to explain PCO_2RR in Fig. 5c [38–49]. To begin with, the PS in the reaction milieu augments the absorption of visible light. Upon exposure to light, photoelectrons in

the PS are stimulated to transition from the HOMO to the LUMO levels. Subsequently, they migrate towards catalyst **1**, facilitated by the matched LUMO alignment. This migration leads to an oxidized state of PS^+ and a reduced state of catalyst **1**. Following this, Intercalated water molecules, as proton donors, promote the electron transfer process of proton coupling. At the same time, the reducing $\{P_4Mo_6{}^V\}$ clusters on catalyst **1** act as "electron sponges", which can efficiently enrich and transfer electrons, thus promoting the efficient conduct of the whole reaction. In parallel, the cobalt active metal site on catalyst **1** captures and activates a CO_2 molecule. Ultimately, the adsorbed CO_2 molecule transforms CO, and the CO product is released from the surface of catalyst **1**. Thereafter, catalyst **1** reverts to its initial photocatalytic configuration, poised to commence another catalytic cycle. The HOMO photogenerated hole of TEOA neutralizing PS acts as a sacrificial reagent to restore PS^+ to its original state and convert itself into $TEOA^+$.

In summary, we constructed POM-based photocatalysts **1** through water intercalation strategies. The CO formation rate of water-intercalated catalyst **1** is 21,347.4 $\mu mol\, g^{-1}\, h^{-1}$, which is 1.68 times that of anhydrous intercalated catalyst **2**, and is better than most reported photocatalysts. The crystal structure analysis and DFT calculation reveal the correlation between the O-Mo-O tilt Angle and the bandgap energy: the larger tilt Angle brings the CB edge and the VB edge closer together. This will provide a new idea for developing crystal reduction cluster catalysts for converting CO_2 by water intercalation in bandgap engineering.

CRediT authorship contribution statement

Yin-Hua Zhu: Writing – original draft, Investigation, Conceptualization. **Yong-Qi Ji:** Investigation, Validation. **Jian-Bo Yang:** Validation. **Xin-Ying Xiang:** Validation. **Hua Mei:** Writing – original draft, Investigation, Conceptualization. **Yan Xu:** Writing – review & editing, Writing – original draft, Validation, Supervision, Investigation.

Declaration of competing interest

The authors declare that they have no known competing financial interests or personal relationships that could have appeared to influence the work reported in this paper.

Acknowledgments

This work was supported by the Natural Science Foundation of China (No. 22571157) and the Cultivation Program for the Excellent Doctoral Dissertation of Nanjing Tech University.

Supplementary materials

Supplementary material associated with this article can be found, in the online version, at doi:10.1016/j.cclet.2025.111412.

References

[1] R. Paul, R. Das, N. Das, et al., Angew. Chem. Int. Ed. 62 (2023) e202311304.
[2] R. Paul, A. Boruah, R. Das, et al., Small 20 (2023) 2305307.
[3] R. Das, R. Paul, A. Parui, et al., J. Am. Chem. Soc. 145 (2022) 422–435.
[4] Y. Xie, Z. Fang, L. Li, H. Yang, T.F. Liu, ACS Appl. Mater. Interfaces 11 (2019) 27017–27023.
[5] H. Yu, E. Haviv, R. Neumann, Angew. Chem. Int. Ed. 59 (2020) 6219–6223.
[6] N. Li, J. Liu, B.X. Dong, Y.Q. Lan, Angew. Chem. Int. Ed. 59 (2020) 20779–20793.
[7] M. Zhang, P. Huang, J.P. Liao, et al., Angew. Chem. Int. Ed. 135 (2023) e202311999.
[8] Y. Zhao, X. Xu, K. Zhang, et al., ACS Catal. 14 (2024) 3556–3564.
[9] X. Sun, L. Sun, G. Li, et al., Angew. Chem. Int. Ed. 61 (2022) e202207677.
[10] Q. Li, J.N. Chang, Z. Wang, et al., J. Am. Chem. Soc. 145 (2023) 23167–23175.
[11] S. Yan, S. Ouyang, H. Xu, et al., J. Mater. Chem. A 4 (2016) 15126–15133.
[12] L.L. Liu, Z.Y. Xu, P. Yi, et al., Chem. Sci. 15 (2024) 16977–16986.
[13] Y.H. Zhu, J.B. Yang, X.M. Liu, et al., Dalton Trans. 51 (2022) 3502–3511.
[14] Y.H. Zhu, J.B. Yang, P.F. Yan, et al., J. Mater. Chem. A 12 (2024) 5340–5347.
[15] S. Li, Y. Peng, C. Hu, Z. Chen, Appl. Catal. B 279 (2020) 119401.
[16] W. Lyu, Y. Liu, J. Zhou, et al., Angew. Chem. Int. Ed. 135 (2023) e202310733.
[17] J.N. Li, Z.Y. Du, N.F. Li, et al., Dalton Trans. 50 (2021) 9137–9143.
[18] J. Du, Y. Ma, X. Xin, et al., Chem. Eng. J. 398 (2020) 125518.
[19] S.L. Xie, J. Liu, L.Z. Dong, et al., Chem. Sci. 10 (2019) 185–190.
[20] L. Wang, D.W. Bahnemann, L. Bian, et al., Angew. Chem. Int. Ed. 58 (2019) 8103–8108.
[21] R. Wang, J. Liu, L.Z. Dong, et al., CCS Chem. 5 (2023) 2237–2250.
[22] Z.Y. Du, Y.Z. Yu, N.F. Li, et al., Sustain. Energy Fuels 5 (2021) 3876–3883.
[23] A. Xia, J. Zheng, Q. Zhang, et al., Chem. Eng. J. 496 (2024) 154381.
[24] Y. Zhao, Z. Shao, Y. Cui, et al., Small 19 (2023) 2300398.
[25] Y. Benseghir, A. Solé-Daura, P. Mialane, et al., ACS Catal. 12 (2021) 453–464.
[26] L. Wang, T. Yang, B. Feng, et al., Chin. J. Catal. 54 (2023) 265–277.
[27] H. Tang, F. Xiong, Y. Jiang, et al., Nano Energy 58 (2019) 347–354.
[28] Y.S. Xia, M. Tang, L. Zhang, et al., Nat. Commun. 13 (2022) 2964.
[29] J. Zou, S. Wu, Y. Lin, et al., Environ. Sci. Technol. 58 (2024) 14895–14905.
[30] G. Chen, Y. Ji, X. Shi, et al., Chem. Eng. J. 496 (2024) 154261.
[31] S. Biswas, F.A. Rahimi, R.K. Saravanan, et al., Chem. Sci. 15 (2024) 16259.
[32] Y. Wang, Z. Qin, M.J. Buehler, Z. Xu, Nat. Commun. 7 (2016) 12854.
[33] L. Li, S. Xu, E.A. Carter, Chem. Mater. 32 (2020) 10678–10687.
[34] X. Yu, C.C. Zhao, J.X. Gu, et al., Inorg. Chem. 60 (2021) 7364–7371.
[35] O. Oulhakem, B. Rezki, M. Belaiche, et al., J. Catal. 427 (2023) 115109.
[36] J. Du, Z.L. Lang, Y.Y. Ma, et al., Chem. Sci. 11 (2020) 3007–3015.
[37] Y. Feng, F. Fu, L. Zeng, et al., Angew. Chem. Int. Ed. 63 (2024) e202317341.
[38] Q. Mi, Y. Ping, Y. Li, et al., J. Am. Chem. Soc. 134 (2012) 18318–18324.
[39] C. Dai, L. Zhong, W. Wu, et al., Solar RRL 6 (2022) 2100872.
[40] X.Y. Dao, W.Y. Sun, Inorg. Chem. Front. 8 (2021) 3178–3204.
[41] M. Dong, Y. Tian, J.X. Gu, et al., Inorg. Chem. Front. 10 (2023) 1279–1285.
[42] L. Bian, L. Liang, Y. Fan, et al., J. Colloid Interface Sci. 671 (2024) 543–552.
[43] H. Tao, T. Jia, L. Zhang, et al., J. Colloid Interface Sci. 655 (2024) 909–919.
[44] T. Jia, L. Wang, Z. Zhu, et al., Chin. Chem. Lett. 35 (2024) 108692.
[45] N. Wang, J. Huang, L. Chen, et al., Chem. Eng. J. 486 (2024) 150273.
[46] Z. Jiang, K. Tong, Z. Li, H. Tao, M. Zhu, Angew. Chem. Int. Ed. 64 (2025) e2025007.
[47] H. Dong, F.M. Zhang, Chin. J. Struct. Chem. 43 (2024) 100307.
[48] J. Ning, J. Huang, Y. Liu, et al., Chin. J. Struct. Chem. 43 (2024) 100453.
[49] J. Ma, L. Li, Y. Zhang, J. Qian, X. Wang, Chin. J. Struct. Chem. 43 (2024) 100466.